Progress In Electromagnetics Research M, Vol. 99, 13–22, 2021

Remote Human Respiration Detection Using Ultra-Wideband Impulse Radar Mounted on a Linearly Flying Platform

Budiman P. A. Rohman[1, 2, *] and Masahiko Nishimoto[1]

Abstract—Non-contact vital sign detection using radar is relevant for many applications. In search and rescue missions in disaster-stricken areas, this technology can be used to non-invasively detect live survivors on the ground. However, in a very large disaster area, a fast and effective detection approach is required. This need has suggested radar mounted on a flying platform such as a drone as the most feasible approach. This task is challenging, since human respiration is weak, and the signal recorded is easily affected by disturbances such as noise and movement of the platform. Therefore, in this study, we propose a signal processing technique to deal with this problem. Human respiration signals modulate a hyperbolic pattern recorded by moving radar because of distance projection, leading us to applying sequential image processing steps and hyperbolic pattern reconstruction to extract respiration signals. A Fourier transform is then applied to seek the respiration frequency component. The results of laboratory experiments show that the proposed method can detect human respiration. As an important note, the flying speed of the platform should be determined carefully to cope with slow human respiration.

1. INTRODUCTION

Remote detection of human respiration using ultra-wideband (UWB) radar is desirable for many applications, including military, medical, and search and rescue missions [1–4]. The use of a drone-borne radar is promising, especially in large areas where observation is risky and complex. The drone provides flexibility and mobility to support this kind of mission. In addition, the modularity of the drone means that different multiple sensors can be employed based on the specific mission [3, 4]. However, the detection of human vital signs using a drone-borne radar is challenging, since the signal of human respiration is weak and easily contaminated by noise. The problem becomes more complex when the drone moves or flies at a certain speed above the human body.

Various radar signal processing techniques for remote vital sign detection have been developed. For example, Xu et al. proposed the use of multiple higher-order cumulants for UWB impulse radar to detect vital signs, specifically using the fourth order cumulant. Testing showed that this method could extract information about distance and respiration frequency [5]. Naishadam et al. applied the state space method to UWB radar echo to detect and estimate cardiac and respiration rates. This method can characterize the vital signal without the higher-order harmonics and intermodulation products that commonly plague Fourier analysis [6]. Then, Wu et al. proposed a signal processing for UWB linear array radar. This method can estimate the azimuth angle and detect multiple respirations from B-scan data [7]. Although the methods outlined here show promise, they need data collected over a relatively long period and work only in static conditions.

There is limited research on the application of such detection methods to non-stationary conditions. Li and Lin proposed the use of two radars working together to accommodate one-dimensional random

Received 2 October 2020, Accepted 16 November 2020, Scheduled 25 November 2020
* Corresponding author: Budiman Putra Asmaur Rohman (budi028@lipi.go.id).
[1] Graduate School of Science and Technology, Kumamoto University, Japan. [2] Research Center for Electronics and Telecommunication, Indonesian Institute of Sciences, Indonesia.

body movement [8]. Although the method works well enough, it is relatively complex to implement and not appropriate for drone-borne radar applications. Nakata et al. employed a phase compensation of the drift of hovering drone for human vital sign detection [9]. This method performs well in laboratory experiments but is limited to only half of the radar wavelength by vertical drifting. Of course, to make the human respiration detection more effective, the flying platform or drone is required despite of hovering. Since the human respiration signal is very weak and slow, a flying drone borne radar needs a robust radar signal processing to tackle this problem.

In this paper, we propose a new detection technique for UWB impulse radar which is mounted on a linearly flying platform, such as drone borne radar searching for human vital signs on the ground. The proposed technique works by employing several sequential techniques, such as adaptive thresholding, image processing, and hyperbolic pattern fitting. Instead of respiration frequency and strength, the study focuses on the effects of platform flying speed and height on its ability to detect a human respiration signal.

2. PROBLEM FORMULATION

The problem formulation is illustrated in Fig. 1. In common static vital sign detection schemes, the radar system detects the changes in target distance corresponding with delay time caused by the respiration and heartbeat. The range between the human chest and radar is defined as

$$x(t) = x_0 + r(t) = x_0 + A_r \ \sin(2\pi f_r t) + A_h \ \sin(2\pi f_h t) \tag{1}$$

where x_0 is a constant distance between radar and human; A_r and A_h are the amplitudes of respiration and heartbeat, respectively; and f_r and f_h are the corresponding frequencies. The propagation time delay $\tau_v(t)$ of this distance can be expressed by

$$\tau_v\left(t\right) = \frac{2x(t)}{c} = \tau_0 + \tau_r \sin\left(2\pi f_r t\right) + \tau_h \sin\left(2\pi f_h t\right) \tag{2}$$

with $c = 3 \times 10^8$ m/s being the speed of light, $\tau_0 = 2x_0/c$, $\tau_r = 2A_r/c$, and $\tau_h = 2A_h/c$. Then, by considering that just one human exists, and all other objects are stationary or not moving, the radar impulse response is given by

$$u\left(\tau, t\right) = a_v \delta\left(\tau - \tau_v\left(t\right)\right) + \sum_i a_i \delta(\tau - \tau_i) \tag{3}$$

where τ is the propagation delay; $a_i\delta(\tau - \tau_i)$ is the signal from the i-th static target with amplitude a_i and time delay τ_i; and $a_v\delta(\tau - \tau_v(t))$ is the human vital sign motion signal with amplitude a_v.

In the case of moving radar or antenna, as illustrated in Fig. 1(a), the propagation delay will follow the hyperbolic pattern caused by radar distance projection (see Fig. 1(b)). Since the hyperbolic shape

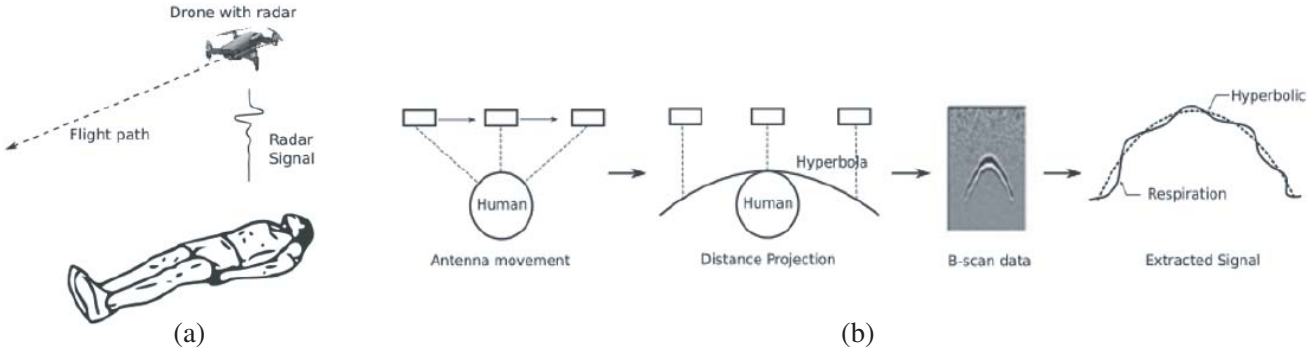

Figure 1. Illustration of (a) vital sign detection on the human lying on the ground, and (b) respiration sign modulate on the hyperbolic pattern.

and size depend on the platform speed and height, we assume that the hyperbolic pattern is a function of time t and one-dimensional space η, $\zeta(t, \eta)$. Thus, the new propagation delay $\tau'_v(t)$ is defined as

$$\tau'_v(t) = \zeta(t, \eta)\, \tau_v(t) \tag{4}$$

Therefore, if $s(t)$ is the transmitted signal, the received signal $R(\tau, t)$ is defined as

$$R(\tau, t) = s(t) * u'(t, \tau) = a_v s\left(t - \tau'_v(t)\right) + \sum_i a_i s(t - \tau_i) \tag{5}$$

Since the heartbeat signal is weak, we focus on the respiration signal in this study. Our method works by locating and estimating $\zeta(t, \eta)$, allowing us to extract the respiration signal pattern $\tau_r \sin(2\pi f_r t)$.

3. PROPOSED METHOD

The proposed detection method consists of four major steps: data acquisition and pre-processing, image processing, hyperbola pattern fitting, and post-processing (see Fig. 2). The result of each processing step can be seen in Fig. 3.

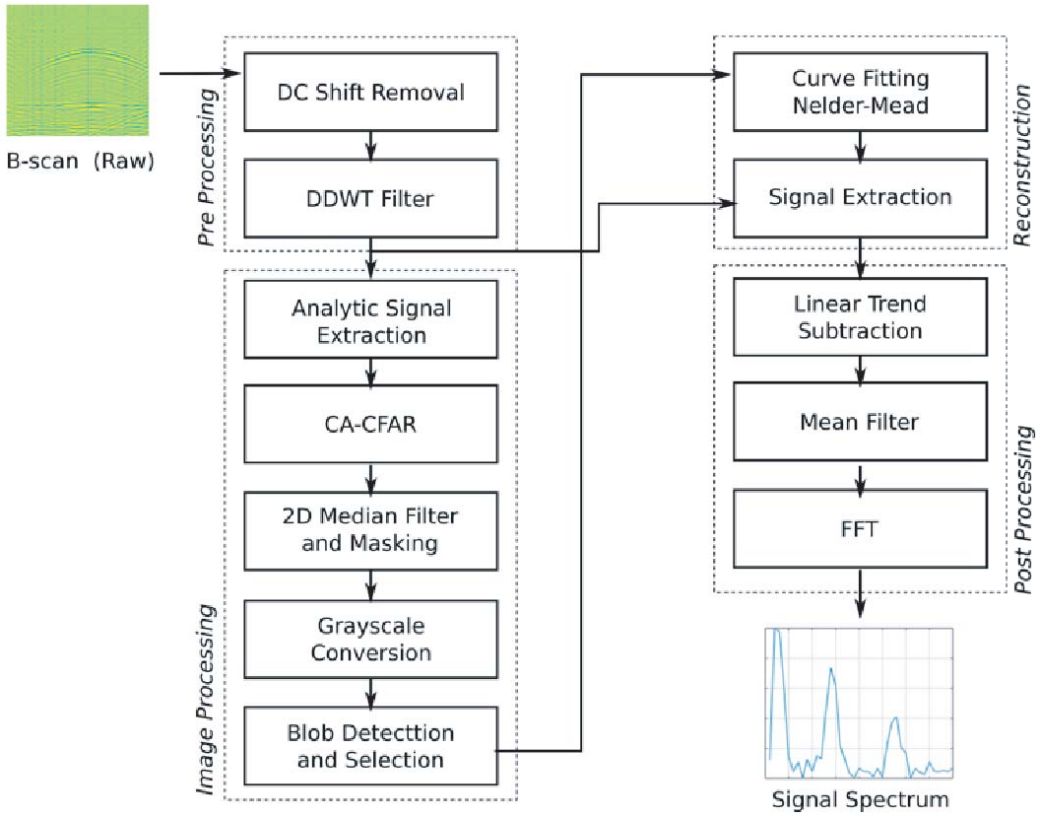

Figure 2. Proposed signal processing technique.

3.1. Data Acquisition and Preprocessing

The radar system records data during the flight. The collected data are R with size $M \times N$, where M and N are the sizes for the fast and slow time domains, respectively. In this case, the fast time domain correlates with the range sampling point, while the slow time domain correlates with distance achieved by the drone flight path containing the respiration signal.

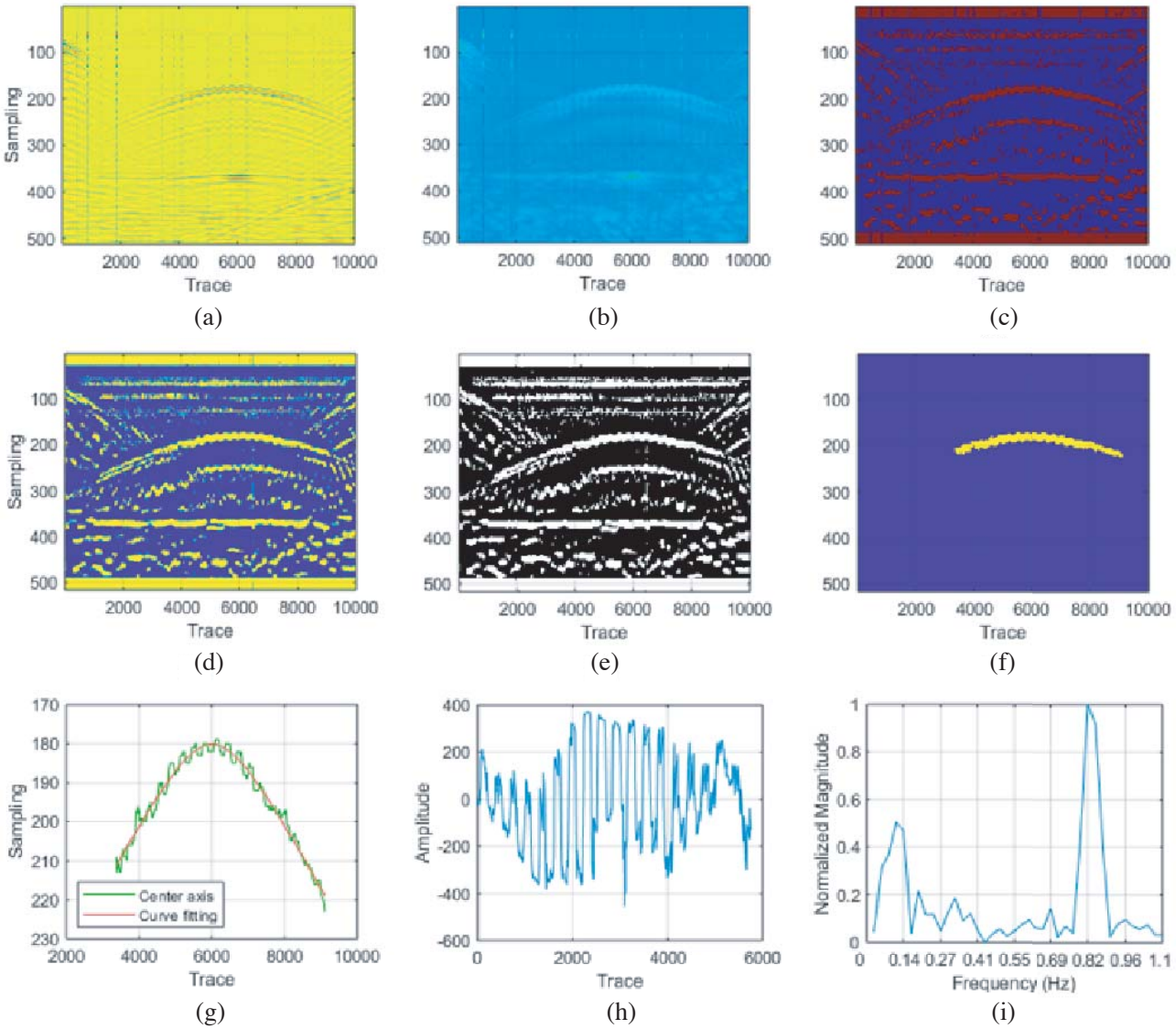

Figure 3. Result in each processing step with laboratory data, respiration frequency 0.8 Hz, displacement 10 mm.

As the first step, the direct-current (DC) bias component of each trace signal is removed. This process is computed by removing the mean value of each trace expressed by

$$\bar{R}[m,n] = R[m,n] - \frac{1}{M}\sum_{m=1}^{M} R[m,n] \tag{6}$$

Then, a double density discrete wavelet transform (DDDWT) filter is applied to denoise the signal. This filter has been previously confirmed to perform well in radar applications [10, 11]. It works by recursively applying the three-channel analysis filter banks to the lowpass sub-band. Conversely, the inverse double-density wavelet transform is obtained by iteratively applying the synthesis filter bank. The filter bank constants were adopted from [10].

$$\Re[m,n] = DDDWT\left(\bar{R}[m,n]\right) \tag{7}$$

This process is necessary to create a clean image for signal thresholding and blob detection process (Fig. 3(a)).

3.2. Image Processing

For thresholding, firstly, we compute the baseband shape of the amplitude of the signal image. Thus, along with the fast time domain, the envelope signal $\Re_s$ was computed from its analytic signal representation through a Hilbert transform H (Fig. 3(b)) expressed by

$$\Re_s(m,n) = |\Re(m,n) + iH\{\Re(m,n)\}| \tag{8}$$

$$H(\Re)(m,n) = \frac{1}{\pi} P.V. \int_{-\infty}^{+\infty} \frac{\Re(k,n)}{(m-k)} dk \tag{9}$$

where *P.V.* is a Cauchy principal value. Then, to extract the segment units of the detected objects, we apply cell-averaging constant false alarm rate (CA-CFAR), which is commonly used in radar applications. CA-CFAR considers two states of signal whether the cell under test contains a target H_1 or not H_0 by maintaining the probability of false alarm P_{fa}, defined as

$$H_1 : r \geq T \tag{10}$$

$$H_0 : r < T \tag{11}$$

where the threshold value T is computed by

$$T = \alpha\ Z \tag{12}$$

$$\alpha = N_{cfar}\left(P_{fa}^{-1/N_{cfar}} - 1\right) \tag{13}$$

with α being a scaling factor, Z the average value of adjacent cells, and N_{cfar} the number of computed adjacent cells. To enhance the object group unity, we choose a relatively high value of P_{fa}. The false detected object area is then removed by the selection step based on the connected pixel size (Fig. 3(c)).

Before the application of blob detection, a two-dimensional median filter and masking filter convolution are applied to remake the image so that the incomplete segment can be united and filled perfectly. If the result of CA-CFAR and median filter is $\bar{\Re}$, the masking filter process is defined as

$$\tilde{\Re}[m,n] = C * \bar{\Re}[m,n] = \sum_{i=-h}^{h} \sum_{j=-h}^{h} C(i,j)\bar{\Re}[m-i, n-j] \tag{14}$$

$$C = \begin{bmatrix} 0 & 0 & 0 & 0 & 0 \\ 0 & 1 & 1 & 1 & 0 \\ 0 & 1 & 1 & 1 & 0 \\ 0 & 1 & 1 & 1 & 0 \\ 0 & 0 & 0 & 0 & 0 \end{bmatrix} \tag{15}$$

where C is the mask kernel matrix with size $h \times h$. The result is shown in Fig. 3(d).

The processed B-scan data are converted to the grayscale image, which is then processed using connected component labeling and selection method to extract the hyperbolic pattern area. This step scans an image and groups its pixels into components based on pixel connectivity. Once all groups have been determined, each pixel is labeled according to the component to which it was assigned ((Fig. 3(e)). Small blobs will be considered noise and removed. The selected blob containing the respiration signal is shown in Fig. 3(f).

The area border of each blob is then smoothed using a moving average technique before making a center axis index to extract the hyperbolic pattern. To minimize inaccuracy in indexing, we calculate the average from the lowest and uppermost values of each time index. This index-connected line roughly represents the axis of the hyperbolic pattern.

3.3. Hyperbolic Pattern Fitting

Since the presence of noise negatively affects the obtained rough hyperbolic axis, the curve fitting method matching the general hyperbolic equation is applied. We employ Nelder-Mead simplex algorithm introduced by Lagarias et al. [12, 13] to refine the pattern. The method is a heuristic optimization algorithm to match the data by applying a gradient-descent method. The success of this fitting method

is determined mostly by the initialization value. The general hyperbolic function is defined in Eq. (16), and Eq. (17) is used for the curve fitting step:

$$\frac{(m-m_0)^2}{a^2} - \frac{(n-n_0)^2}{b^2} = 1 \tag{16}$$

$$m_{est} = a\left(\sqrt{\frac{(n-n_0)^2}{b^2}+1}\right) + m_0 \tag{17}$$

where m and n are the indices of rough hyperbolic pattern axis; m_0 and n_0 are the coordinate index of hyperbolic center; a and b are hyperbolic constants; and m_{est} is the estimated index. In this case, we apply curve fitting to find the optimum values of m_0, n_0, a, and b. The objective function J is defined as

$$J = \sum_{i=1}^{l} \{m - m_{est}\} \tag{18}$$

with l being the length of the blob being tested. From this step, assume that the estimated indices of selected blob were listed as m_{est} and n_{est} so that the reconstructed signal can be represented as $\Re[m_{est}, n_{est}]$. The result of this processing step is shown in Fig. 3(g). From this figure, we confirm the work of the algorithm in the reconstruction of recorded hyperbolic pattern.

3.4. Postprocessing

After obtaining the signal, we apply linear trend subtraction (LTS) to remove the noise and clutter effect, including radar instability and inaccuracy of the hyperbolic pattern reconstruction.

$$\acute{\Re} = LTS(\Re[m_{est}, n_{est}]) \tag{19}$$

We then apply a median filter to smooth the signal producing $\check{\Re}$ so that we can inspect a signal representing human respiration from the frequency component through Fourier transform result expressed by,

$$Y(\omega) = \sum_{i=1}^{l} \check{\Re}(m_{est,i}, n_{est,i}) e^{-j2\pi\omega i/l} \tag{20}$$

with ω being the frequency bin. The result of these processing can be seen in Figs. 3(h)–(i).

4. EXPERIMENTAL SETUP

The experimental setup and equipment are shown in Fig. 4. As radar, we used UWB impulse radar Cayenne from Xethru [14]. A bow-tie antenna pair is used to transmit a monocycle pulse with a bandwidth of 1.5–6 GHz. The sampling rate of the pulse is 39 Giga samples per second. Each of the datasets consists of 5000–6000 traces; each trace has 512 samples, and the rate is around 250 pulses per second. In controlled environment experiments, we used an artificial vital sign actuator developed specially to imitate human chest with displacement of 3, 5, and 10 mm and a frequency of 0.3, 0.6, and 0.8 Hz. These parameters follow the established characteristics of common human respiration [15, 16]. The corresponding speed of the radar movement is around 0.12, 0.08, 0.06, and 0.04 m/s; the range between the radar and respiration actuator is within 1 m.

To confirm the applicability of the method, we also check the method with a real human around 1 m from the radar source. The human respiration frequency is around 0.33 Hz, and its strength is relatively normal.

5. RESULT AND DISCUSSION

5.1. Experiment with Respiration Actuator

The result of the proposed signal processing technique is shown in Fig. 5. Fig. 5(a) shows that when there is no respiration movement, we can see the frequency component from the hyperbolic pattern

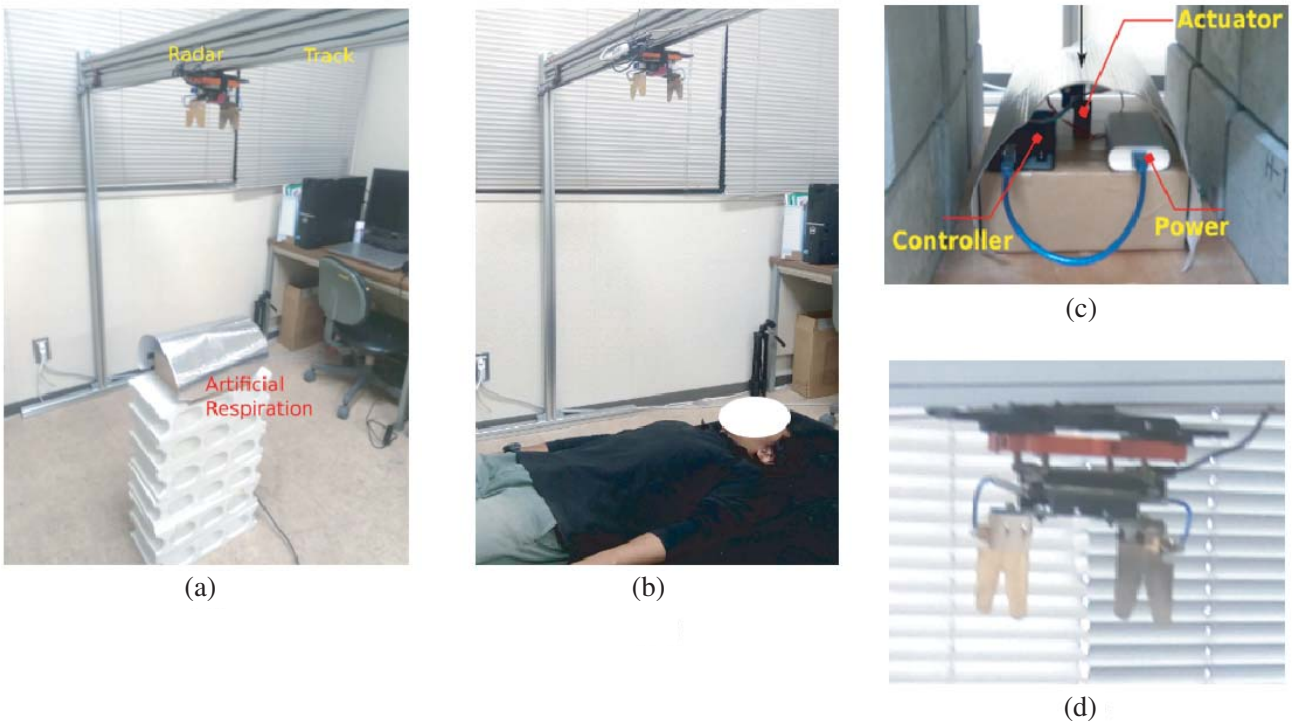

(a) (b) (c) (d)

Figure 4. Experimental setup: (a) measurement using respiration actuator, (b) real human, (c) respiration actuator and (d) radar mounting.

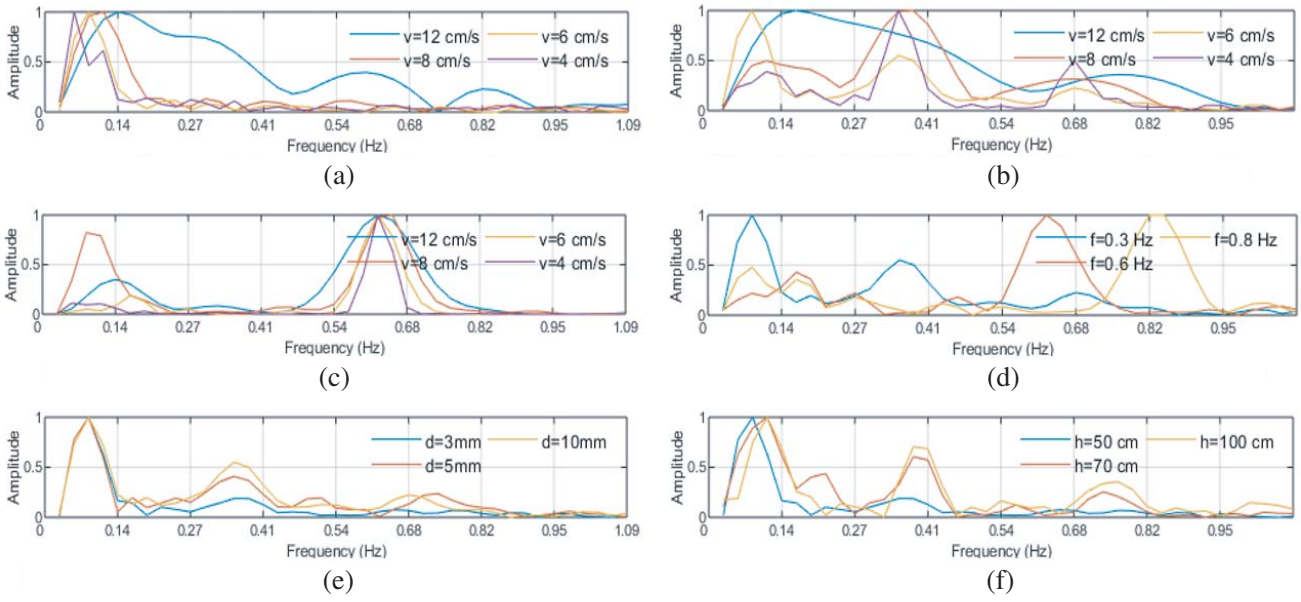

(a) (b) (c) (d) (e) (f)

Figure 5. Result of laboratory experiment with artificial respiration in various parameters: range between radar and object h, respiration frequency f, displacement d, and platform flying speed v. (a) No respiration, $h = 50\,\text{cm}$, various speeds. (b) Respiration $f = 0.3\,\text{Hz}$, $d = 10\,\text{mm}$, $h = 50\,\text{cm}$, various speeds. (c) Respiration $f = 0.6\,\text{Hz}$, $d = 10\,\text{mm}$, $h = 50\,\text{cm}$, various speeds. (d) Respiration $d = 10\,\text{mm}$, $h = 50\,\text{cm}$, $v = 6\,\text{cm/s}$, various frequencies. (e) Respiration $f = 0.3\,\text{Hz}$, $h = 50\,\text{cm}$, $v = 6\,\text{cm/s}$, various displacements. (f) Respiration $f = 0.3\,\text{Hz}$, $d = 3\,\text{cm}$, $v = 6\,\text{cm/s}$, various heights.

because of distance projection. The frequency component in this condition is widened as the platform speed increases. This means that this component will overlap and mask the respiration signal at very high speed, as confirmed in Fig. 5(b). At very high speed (12 cm/s), the respiration signal component is fully masked (Fig. 5(b)).

The speed of the radar also affects the recorded respiration signal. As shown in Fig. 5(c), higher speed produces spectral leakage wider than the original respiration frequency component. In other words, with high radar speed, the accuracy of respiration frequency estimation decreases.

Figures 5(c) and (d) show that detection is more feasible when the respiration frequency is higher. In addition, instead of being masked by the hyperbolic component, the low-frequency respiration is easily masked by background noise. Fig. 5(e) compares the result of the proposed method with different respiration displacements. This parameter imitates the strength of human respiration. This figure shows that under the same conditions, weak respiration is more easily distorted, with low magnitude of the frequency component. Thus, it is possible that weak and slow respiration may not be detected.

We analyze the height effect (Fig. 5(f)). A range increase makes the respiration signal clearer, confirmed by the peakness of magnitude of the frequency component. This may be caused by inter-reflection between the radar and the object. Thus, from this result, a range of around 1 m is recommended.

In most cases, the measured frequency components are a little higher than the actual condition, which may be caused by the inaccuracy of axis transformation of a hyperbola. Unstable data acquisition processing may also be a reason for this shift. The limited sample data used to represent the respiration signal may have also contributed to this issue. However, compared to no-respiration condition, the results above confirm the function of the proposed method in the detection scheme.

5.2. Experiment with Real Human

We also conduct a laboratory experiment using a human (Fig. 6). Since the human body is not as reflective as a respiration actuator in our previous section, the recorded signal seems weaker.

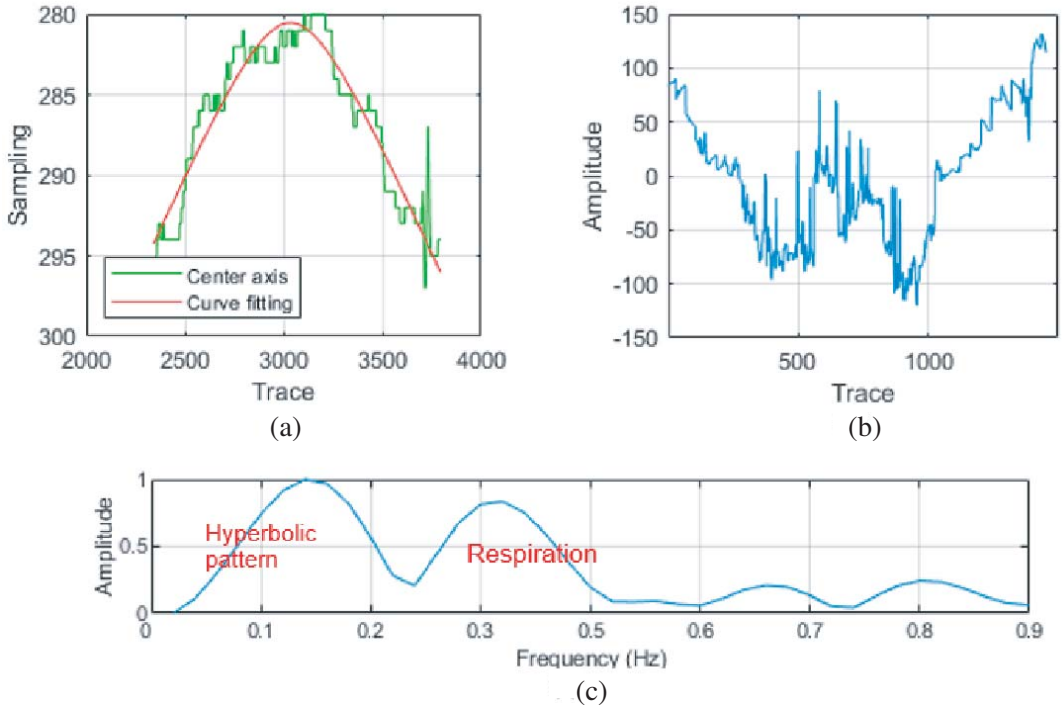

Figure 6. Result of laboratory experiment with real human, $v = 6$ cm/s, $h = 80$ cm: (a) reconstruction of hyperbolic pattern, (b) time domain signal, (c) frequency domain signal.

However, the proposed method still works well and is able to extract the blob representing a human for further inspection and extraction of the time-domain signal (Figs. 6(a)–(b)). Then, through frequency component analysis, we are still able to detect respiration, despite its relative broadness due to weak reflection and short recording period (Fig. 6(c)). Configuring the platform speed will be a crucial part since the faster speed will make the frequency component of respiration and hyperbolic pattern overlap as we shown in the result of experiment with actuator (Fig. 5(b)). Overall, this result confirms the applicability of our proposed method for detecting real humans.

6. CONCLUSION

We describe our proposed technique for UWB impulse radar mounted on a flying platform to non-invasively detect human respiration from a person on the ground. Controlled environment laboratory experiments by using both respiration actuator and real human indicate the effectiveness of this method.

The results of this study suggest that the proposed method may be appropriate for detecting live disaster survivors on the ground. Although the speed of the flying platform should be relatively slow, this limitation can be tackled by appropriate drone equipment choices. For example, we can use dual sensors on the drone employing radar and a forward-looking camera. In the beginning, the drone will fly at a normal speed, but when the camera detects possible survivors, the drone could reduce its speed and record radar echo to attempt to detect respiration sign existence.

However, some limitations in this method should be considered. First, in this study, we focus on one person as a target for one-time processing. Multiple person detection is possible by using our method, but it requires a sequential process. Second, in this study, we assume that the platform flies linearly. Since we used a directional antenna so that a nonlinear and uncontrolled flying behavior may reduce the clarity of the recorded signal. In the worst case, the vital sign will not be recorded. Nevertheless, the data recording duration of each person is relatively short, thus linear flying in that time is very possible except that there is any significant disturbance such as strong wind or unreliable controller.

The human buried by building debris case is also possible, but the advancement of the method is required since in that case, several issues should be considered such as reflection and attenuation of the signal. Future work should focus on such a situation.

REFERENCES

1. Ralf, B., et al., "UAV-based polarimetric synthetic aperture radar for mine detection," *2019 IEEE International Geosciences and Remote Sensing Symposium*, 9208–9211, IEEE, 2019.
2. Feng, Q., J. Liu, and J. Gong, "UAV remote sensing for urban vegetation mapping using random forest and texture analysis," *Remote Sensing*, Vol. 7, No. 1, 1074–1094, 2015.
3. Rohman, B. P. A., et al., "Multisensory surveillance drone for survivor detection and geolocalization in complex post-disaster environment," *2019 International Geosciences and Remote Sensing Symposium 2019*, 9368–9371, IEEE, 2019.
4. Andra, M. B., B. P. A. Rohman, and T. Usagawa, "Feasibility evaluation for keyword spotting system using mini microphone array on UAV," *2019 International Geosciences and Remote Sensing Symposium 2019*, 2264–2267, IEEE, 2019.
5. Xu, Y., et al., "Vital sign detection method based on multiple higher order cumulant for ultrawideband radar," *IEEE Transactions on Geoscience and Remote Sensing*, Vol. 50, No. 4, 1254–1265, 2013.
6. Naishadham, K., et al., "Estimation of cardiopulmonary parameters from ultra wideband radar measurements using the state space method," *IEEE Transactions on Biomedical Circuits and Systems*, Vol. 10, No. 6, 1037–1046, 2016.
7. Wu, S., et al., "Study on a novel UWB linear array human respiration model and detection method," *IEEE Journal of Selected Topics in Applied Earth Observations and Remote Sensing*, Vol. 9, No. 1, 125–140, 2016.

8. Li, C. and J. Lin, "Complex signal demodulation and random body movement cancellation techniques for non-contact vital sign detection," *2008 IEEE MTT-S International Microwave Symposium Digest*, 567–570, IEEE, 2008.
9. Nakata, R. H., et al., "Motion compensation for an unmanned aerial vehicle remote radar life sensor," *IEEE Journal on Emerging and Selected Topics in Circuits and Systems*, Vol. 8, No. 2, 329–337, 2018.
10. Selesnick, I. W., "The double density discrete wavelet transform," *Wavelets in Signal and Image Analysis: From Theory to Practice*, Springer, Netherlands, 2001.
11. Baili, J., et al., "Application of the discrete wavelet transform to denoise GPR signals," *2nd International Symposium on Communications, Control and Signal Processing*, 2006.
12. Lagarias, J. C., J. A. Reeds, M. H. Wright, and P. E. Wright, "Convergence properties of the Nelder-Mead simplex method in low dimensions," *SIAM Journal of Optimization*, Vol. 9, No. 1, 112–147, 1998.
13. Nelder, J. A. and R. Mead, "A simplex method for function minimization," *The Computer Journal*, Vol. 7, 308–313, 1965.
14. Cayenne Radar Development Kit — Bow Tie, Available online: https://store.flatearthinc.com/products/cayenne-radar-development-kit (accessed on 26 September 2019).
15. Lindh, W. Q., et al., *Delmar's Comprehensive Medical Assisting: Administrative and Clinical Competencies*, Cengage Learning, New York, 2013.
16. Kondo, T., et al., "Laser monitoring of chest wall displacement," *European Respiratory Journal*, Vol. 10, No. 8, 1865–1869, 1997.